Reconstructing magnetic fields of spiral galaxies from radiopolarimetric observations

Shneider, C.

Citation

Shneider, C. (2015, December 17). *Reconstructing magnetic fields of spiral galaxies from radiopolarimetric observations*. *PhD Thesis*. Retrieved from https://hdl.handle.net/1887/37053

2

Power spectra of synchrotron radio observables with Faraday effects and turbulent magnetic field

C. Shneider, M. Haverkorn, A. Fletcher

Astronomy & Astrophysics, 2015
To be submitted

Abstract

We simulate a typical high Galactic latitude interstellar medium (ISM) environment with characteristic regular $B = 3\,\mu$G and turbulent $b = 6\,\mu$G magnetic field strengths and both thermal and cosmic ray electron densities. The solenoidal, random Gaussian magnetic field has a tunable spectral index α_b. We observe this synchrotron emitting and Faraday rotating magneto-ionic medium at a frequency of 350 MHz over a generic path length of 1 kpc with a realistic cone-like field of view which is integrated along the line of sight to yield Stokes I, Q, U, and P maps with power spectra over a multipole range of $150 \leq \ell \leq 1000$. A power spectrum analysis PS(ℓ) is performed on the resulting maps for physically motivated values of α_b. We find that

total synchrotron intensity is a good tracer of the spectral index of the turbulent magnetic field whereas spectral indices of polarized intensity and of the Stokes parameters cannot be used as these depend degenerately on many factors characterizing the medium. We find a frequency dependent break in the polarized intensity and Stokes parameters which occurs at smaller angular scales for lower frequencies.

2.1 Introduction

Efforts to characterize the turbulent magneto-ionic medium of our Galaxy from synchrotron radio emission and its linear polarization spanning centimeter to meter wavelengths, originate from the Wieringa et al. (1993) discovery of small scale structure in this emission at 325 MHz using the Westerbork Synthesis Radio telescope (WRST). The production of synchrotron radiation throughout the Galactic volume and its depolarization (Burn 1966; Sokoloff et al. 1998, 1999, and Chap. 3 of this thesis) by the intervening plasma - the interstellar medium (ISM) - along essentially every line of sight through the Galaxy, provides information on the spatial distribution of the thermal and cosmic ray electron densities and strength of Galactic magnetic fields. This information is also important for cosmic microwave background (CMB) polarization B-mode detection (Carretti et al. 2010), for high-resolution extragalactic observations with the SKA (Sun & Reich 2009), as well as epoch of reionization (EoR) studies (Jelić et al. 2008).

At wavelengths of just a few centimeters, the measured (diffuse) polarization directly traces the magnetic field in the emitting region because Faraday rotation is negligible whereas at longer wavelengths additional information on magnetic field structure and electron density along the entire line of sight is obtained. Faraday rotation refers to the rotation of the intrinsic polarization vector from its angle, on emission, by an amount proportional to the square of the observing wavelength. The proportionality constant is the rotation measure (RM)

$$RM = 0.81 \int_{\mathrm{source}}^{\mathrm{observer}} n_{\mathrm{e}} \, (B_{||} + b_{||}) \, dl,$$

which is comprised of the thermal electron density n_{e} (cm^{-3}), the regular $B_{||}$ and random $b_{||}$ components of the magnetic field (μG) directed along the line of sight, and the path length (pc) through the ionized ISM. Owing to the presence of both regular and random Galactic magnetic field components in the disk and halo together with thermal and cosmic ray electrons, Faraday rotation causes depolarization by differential Faraday rotation (DFR) (also known as depth depolarization) and depolarization by Faraday dispersion (FD) (also referred to as beam depolarization).

Consequently, a subset of existing radio polarization surveys, ranging from several hundred MHz to a few GHz frequencies and covering many different parts of the sky at various spatial and angular scales, have been analyzed using power spectra (PS), angular power spectra (APS), and structure functions SFs in order to parametrize structure in radio maps of total synchrotron intensity I, Stokes parameters Q and U (or in CMB studies, the E- and B- modes, respectively (Tucci et al. 2002)), and polarized intensity P. PS use a (planar) fast Fourier transform (FFT) on a Cartesian grid, APS use a spherical harmonic expansion on a spherical grid, and SFs are a measure of autocorrelation used to study random processes whose power spectra are given by a power law (Simonetti et al. 1984) and do not require a regular grid of data points as do both PS and APS (Haverkorn et al. 2003). Haverkorn et al. (2003) also studied both power spectra and structure functions of diffuse polarization in the Galaxy from RM maps. Most of these surveys focus on low Galactic latitudes although there is observational evidence for significant RM structure at high Galactic latitudes ($b \sim 71^\circ$) at low frequencies (315−388 MHz) (de Bruyn et al. 2006) and possibly at high frequencies (1.4 GHz) from simulations of (Sun & Reich 2009). Significant magnetic field strengths are also present in the Galactic halo (Haverkorn & Heesen 2012). For a compilation and application of PS, APS, and SFs to these various surveys see Stutz et al. (2014, and refs. therein) and Haverkorn et al. (2003). Present surveys with the Low Frequency Array (LOFAR) such as the Multifrequency Snapshot Sky Survey (MSSS) (Heald & LOFAR Collaboration 2014), surveys by the Murchison Widefield Array (MWA) (Bowman et al. 2013), and future surveys such as by the Square Kilometre Array (SKA) will be able to reveal polarized structure at frequencies as low as several tens of MHz making detailed study of the Galactic halo at low frequencies possible.

However, the interpretation of the values of the power spectra of I, Q, U, P and RM is still uncertain. The difficulty comes from the dependence of these observables on magnetic field structure and direction, thermal electron density distribution and path length. The magnetic field fluctuations are coupled to the thermal electron fluctuations which follow a power law extending over ten orders of magnitude (Armstrong et al. 1995; Chepurnov & Lazarian 2010). From here on, α_X represents the angular power spectral index of a parameter X. A given angular scale θ, measured in degrees, is related to the multipole number ℓ that would be obtained by a spherical harmonic transform of spherically gridded data, through the relation $\ell \approx 180^\circ/\theta$ (Haverkorn et al. 2003; Stutz et al. 2014). Spectral indices of polarized intensity vary widely ($0.7 \lesssim \alpha_\mathrm{P} \lesssim 3$) for $\ell \approx 10$ to $\ell \approx 6000$ among surveys at different frequencies and Galactic longitude and latitude (Haverkorn et al. 2003). La Porta & Burigana (2006) find $1 \leq \alpha_\mathrm{P} \leq 1.5$ at 408 MHz to $2 \leq \alpha_\mathrm{P} \leq 3$ at 1.4 GHz for $10 \leq \ell \leq 100$. However, Stutz et al. (2014) showed that at the single frequency of 1.4 GHz, α_P also shows variations from about 0.7 to 4 along the Galactic plane for $\ell \approx 60$ to $\ell \approx 10^4$. α_P varies with Galactic latitude, tracing the disk, halo, and disk-halo transition but no correlation with Galactic longitude is found (Stutz et al. 2014; Haverkorn et al. 2003). α_I is dominated by large scale structure and varies in roughly the same range as α_P with $0.4 \lesssim \alpha_\mathrm{I} \sim 2.2$ or ~ 3.0 but $\alpha_\mathrm{I} \simeq 0$ where extragalactic point sources dominate (Baccigalupi et al. 2001; Bruscoli et al. 2002). La Porta et al. (2008) find $2.5 \leq \alpha_\mathrm{I} \leq 3$ for $\ell \lesssim 200$. Observationally, there is no clear relationship between α_I and α_P (Baccigalupi et al. 2001). Many interferometric surveys do not have reliable α_I due to missing large scale variation in I but do have reliable α_P. Furthermore, power spectral indices of Stokes parameters Q and U are found to strongly correlate with α_P (Stutz et al. 2014, see Fig. 8).

As a first-approach to the problem of interpreting the broad range of observed power spectral indices, our aim is to discern trends between the power spectral index of the turbulent magnetic field α_b and the power spectral indices of the parameters of synchrotron radiation $\alpha_{\mathrm{I}}, \alpha_{\mathrm{Q}}, \alpha_{\mathrm{U}}$, and α_{P} in the context of a generalized high Galactic latitude environment. In this chapter, polarized structure is produced in numerical models by having an isotropic turbulent (random) magnetic field with a non-zero energy spectrum dominate over the regular field throughout the entire synchrotron emitting and Faraday rotating volume. The regular field is separately oriented parallel and then perpendicular to the line of sight. We also determine the effect on the power spectral indices $\alpha_{\mathrm{I}}, \alpha_{\mathrm{Q}}, \alpha_{\mathrm{U}}$, and α_{P} caused by incorporating assumptions of point-wise equipartition/pressure equilibrium between cosmic ray electrons and local total magnetic field and likely level of anti-correlation between cosmic ray electron density and magnetic energy density into our models.

In Sect. 2.2 we describe the physical model chosen for the Galactic ISM, the modeling of magnetic field configurations, the correlation of cosmic ray electron density with the magnetic energy density, and arrive at synthetic maps of the Stokes parameters from independent realizations using diverging lines of sight with subsequent angular power spectrum analysis performed on these maps. We present and discuss results in Sections 2.3 and 3.7 and finally present conclusions in Section 2.5.

2.2 Model description

We consider the Galactic ISM at typical high Galactic latitudes, with short 1 kpc and 2 kpc sight lines, in order to avoid influence from discrete objects such as H II regions, which are concentrated in the disk, and model a synchrotron emitting and Faraday rotating, magneto-ionic medium. Since we are interested in small scale structure in polarization caused by both depth depolarization and beam depolarization we choose a low ‘observing’ frequency of 350 MHz. This is a typical frequency where polarized has been observed as in (Haverkorn et al. 2003). We further compare our results at 350 MHz with frequencies of 1 GHz, 700 MHz, 500 MHz, 200 MHz and 50 MHz and also consider the case where no Faraday rotation occurs.

The standard input parameters in this model are: a regular magnetic field B (μG) which is separately taken as being parallel and perpendicular to the line of sight ($B_{||}, B_{\perp}$), an isotropic turbulent magnetic field b (μG), a maximum turbulent cell size d (pc), and both thermal and cosmic ray electron densities (cm^{-3}).

We adopt a regular magnetic field strength of $3\,\mu$G and add it to the turbulent magnetic field to have a regular field oriented parallel to the line of sight $\boldsymbol{B}_{\mathrm{tot}} = \boldsymbol{B}_{||} + \boldsymbol{b}$, perpendicular to the line of sight $\boldsymbol{B}_{\mathrm{tot}} = \boldsymbol{B}_{\perp} + \boldsymbol{b}$, or with $\boldsymbol{B}_{\mathrm{tot}} = \boldsymbol{b}$ (regular field absent). The isotropic turbulent magnetic field has a root mean square (rms) field strength (with mean zero), given by its standard deviation, is fixed to $\sigma_b = 6\,\mu$G with each component $\sigma_{b_i} = (6/\sqrt{3})\,\mu$G where $i = x, y, z$. Moreover, the turbulent field has a power spectrum given by a power law with an adjustable spectral index α_b. The regular magnetic field strength and isotropic turbulent magnetic field strength that are used are comparable with values obtained earlier in the literature: for the regular field $B \sim 2\,\mu$G (Zweibel & Heiles 1997; Sun & Reich 2009) or $B \sim 4\,\mu$G (Zweibel & Heiles 1997; Schnitzeler 2008) and for the turbulent field in the halo $\sigma_b \leq 6\,\mu$G (Jansson & Farrar 2012) or the slightly more conservative estimate $\sigma_b \sim 3\,\mu$G assumed in (Sun & Reich 2009). A value of 100 pc is used for the maximum turbulent cell size. We adopt $n_\mathrm{e} = 0.014$ cm^{-3} from the value found by Gaensler et al. (2008). Whereas n_e is a constant, the cosmic ray electron density may fluctuate about its constant mean value with $\delta_{n_\mathrm{cr}} = 0.2$. Based on Haverkorn et al. (2004, Appx. B) for our values of the the path length and observing frequency, we choose $c = 0.6$ where c is a constant proportional to the cosmic ray electron density n_cr. The square of the total magnetic field is also correlated with n_cr with the correlation parameter C taking on values of $(-1, -0.5, 0, +0.5, +1)$.

We simulate a box of $128 \times 128 \times (640, 1280)$ pixels, where the 640 and 1280 pixels are along the line of sight and represent 1 kpc and 2 kpc, respectively. Then, the field of view is $11^\circ.3$ and $5^\circ.7$, both corresponding to a distance of 200 pc at the far side of the simulation volume (short edge of the box). This gives corresponding angular resolutions of 0.18° and 0.09° per pixel, accounting for the Nyquist sampling frequency which requires 2 pixels per wave. Thus, by construction, the available ℓ range is $31 \leq \ell \leq 1005$ and $63 \leq \ell \leq 2011$ in our simulations which allows for comparison with power spectra in Haverkorn et al. (2003); Stutz et al. (2014).

2.2.1 Random magnetic field

We generate a divergence-free, random, isotropic Gaussian magnetic field with a prescribed energy power spectrum following a similar construction as used for chaotic or turbulent flow modeling (Malik & Vassilicos 1999; Wilkin, S. L. 2006; Wilkin et al. 2007) but with aperiodic boundary conditions. The random vector field $\boldsymbol{b} = (b_x, b_y, b_z)$ is position dependent only and is given as the sum over the N modes of the simulation by

$$\boldsymbol{b}\,(\boldsymbol{x}) = \sum_{n=1}^{N} \left[\boldsymbol{F}_n \times \hat{\boldsymbol{k}}_n \cos\left(\boldsymbol{k}_n \cdot \boldsymbol{x}\right) + \boldsymbol{G}_n \times \hat{\boldsymbol{k}}_n \sin\left(\boldsymbol{k}_n \cdot \boldsymbol{x}\right)\right]. \tag{2.1}$$

Each unit vector

$$\hat{\boldsymbol{k}}_n = \begin{pmatrix} \cos\theta \sin\phi \\ \sin\theta \sin\phi \\ \cos\phi \end{pmatrix}$$

and its corresponding wave vector $\boldsymbol{k}_n = k_n \hat{\boldsymbol{k}}_n$ is constructed by selecting at each n a pair of angles (θ, ϕ) randomly from the range $0 \leq \theta < 2\pi, 0 \leq \phi \leq \pi$ such that the pair describes a random point that has equal probability of being chosen in any small area on the surface of a unit sphere. This is achieved by setting

$$\begin{aligned} \theta &= 2\pi u, \\ \phi &= \arccos(2v - 1), \end{aligned}$$

with random variables u, v picked from a uniform distribution on the open interval $(0, 1)$ (Weisstein 2002). It is apparent from Eq. (2.1) that the vector field is solenoidal since $\nabla \cdot \boldsymbol{b} = 0$ is satisfied by construction since $\boldsymbol{k} \cdot (\boldsymbol{X} \times \boldsymbol{k}) = 0$ for any vector $\boldsymbol{X}$. The wave number k_n is constrained by the resolution through $k_n = 2\pi/l_n$, where l_n is the wavelength of the sinusoidal mode n. The smallest wave number (largest scale) k_1 is given by the number of turbulent cells selected for the box of 128^3 pixels and the largest wave number (smallest scale) k_N is constrained by $2\pi/\,(5/128)$ where 5 is the minimum number of pixels needed to resolve a wave. The directions of the vectors $\boldsymbol{F}_n$ and $\boldsymbol{G}_n$ are chosen randomly with the constraint that they be normal to $\boldsymbol{k}_n$ which ensures that the mean energy of each mode is $\left(F_n^2 + G_n^2\right)/2$. The individual modes comprising the magnetic field thus have independent random phases and directions and the amount of energy contained in each mode of the magnetic field is controlled by the lengths of the vectors $\boldsymbol{F}_n$ and $\boldsymbol{G}_n$. The magnitudes of $\boldsymbol{F}_n$ and $\boldsymbol{G}_n$ are defined as

$$F_n = G_n = \left[\frac{2}{3} E\left(k_n\right) \Delta k_n\right]^{1/2},$$

where

$$\Delta k_n = \begin{cases} \left(k_{n+1} - k_n\right)/2 & \text{if } n = 1, \\ \left(k_{n+1} - k_{n-1}\right)/2 & \text{if } 2 \leq n \leq N-1, \\ \left(k_n - k_{n-1}\right)/2 & \text{if } n = N, \end{cases}$$

and $E(k_n)$ is the energy spectrum of the inertial range. For our purpose, we assume a power law energy spectrum of the form $E(k_n) = A\left(k_n/k_1\right)^{-\alpha}$ with $\alpha = 3/2$, $5/3$[1], and 2 and mode independent constant A. These values for the slope are physically motivated by predictions from incompressible and compressible magnetohydrodynamic (MHD) turbulence (Cho & Lazarian 2003; Galtier et al. 2005; Beresnyak & Lazarian 2006; Beresnyak 2014) and are chosen to examine the imprint of both steeper and shallower magnetic field spectra with respect to the expected spectrum of $\alpha_b = 5/3$ on $\alpha_{\rm I}, \alpha_{\rm Q}, \alpha_{\rm U}$, and $\alpha_{\rm P}$. In particular, we set $N = 256$ to have a dense sampling of the energy associated with the inertial turbulence range between k_1 and k_N and merge 20 such independent realizations to make the final simulation cubes b_x, b_y, b_z isotropic. A total of 50 such independent simulation cubes, each of which is $128 \times 128 \times 128$ pixels, are generated for each magnetic field component (b_x, b_y, b_z) for each spectral index examined. This, therefore, allows for the 1 kpc and 2 kpc path lengths to be modeled with 10 and 5 statistically independent line-of-sight volumes, respectively. The standard deviation of the resulting spectral indices of the synthetic maps of I, Q, U, P obtained for each of these independent lines of sight is then taken as the error in the spectral index values.

2.2.2 Correlation method

We test whether the parameters I,Q,U, and P can trace correlations or anti-correlations between the magnetic energy density and cosmic ray electron density following Stepanov et al. (2014). For this purpose, we consider a cosmic ray electron density distribution $n_{\rm cr}$,

---

[1] In the literature, there appear references to a Kolmogorov spectrum for the magnetic field. We emphasize here that a Kolmogorov spectrum strictly refers to the fluctuations of thermal electron density in the local ISM for scales ranging from 10^{-3} AU to 30 pc (Armstrong et al. 1995). A reasonable but unproven assumption states that because turbulent magnetic fields are frozen into the ionized interstellar medium they should follow the Kolmogorov spectrum on these scales (Han 2009).

which fluctuates around its mean value $n_{\mathrm{cr},0}$, given by

$$n_{\mathrm{cr}} = n_{\mathrm{cr},0}\left[1+\delta_{n_{\mathrm{cr}}}\left(C\,\frac{B_{\mathrm{tot}}^2-\overline{B_{\mathrm{tot}}^2}}{\sigma_{B_{\mathrm{tot}}^2}}+\sqrt{1-C^2}\,\frac{W-\overline{W}}{\sigma_W}\right)\right], \tag{2.2}$$

where $\delta_{n_{\mathrm{cr}}} \equiv (\sigma_{n_{\mathrm{cr}}}/n_{\mathrm{cr},0}) = 0.2$ is the relative magnitude of cosmic ray number density fluctuations and σ_X denotes the standard deviation of a variable X, the over-bar denotes ensemble averaging, $\boldsymbol{B}_{\mathrm{tot}} = \boldsymbol{B}+\boldsymbol{b}$ is the total magnetic field, and W is an auxiliary positive-definite, scalar random field which is uncorrelated with the magnetic energy density B_{tot}^2. The correlation parameter C is defined as

$$C = \frac{\overline{n_{\mathrm{cr}}B_{\mathrm{tot}}^2} - n_{\mathrm{cr},0}\overline{B_{\mathrm{tot}}^2}}{\sigma_{n_{\mathrm{cr}}}\,\sigma_{B_{\mathrm{tot}}^2}}.$$

Equipartition and pressure equilibrium are introduced via setting $C = 1$ and $C = -1$ respectively. A shortcoming of applying this method is that negative values of n_{cr} arise when $C < 0$ (in certain realizations at certain locations) because B_{tot}^2 can attain arbitrarily large values (as a Gaussian random variable squared). The maximum percentage of all such negative values attained from all trials is less than 0.03% for $C = -1$ and less than 0.01% for $C = -0.5$ of the total line-of-sight volume. These negative values of n_{cr} are then set to zero in the numerical calculation. This makes an *exact* anti-correlation between n_{cr} and B_{tot}^2 impossible. However, the actual affect of this truncation of negative values on the power spectrum is negligible.

2.2.3 Stokes parameters

Maps of I,Q,U, and P are obtained through numerical integration of the line-of-sight volume using the composite trapezoidal rule. These maps are not convolved with any beam profile at any stage. Sight lines originate in the center of a short edge of the simulation box and diverge to simulate a cone-like field of view using a cubic spline interpolation method. We have,

$$\begin{aligned}
I(x_\perp) &= \int_0^L \varepsilon(\boldsymbol{x})\,dz,\\
Q(x_\perp) &= \int_0^L \varepsilon(\boldsymbol{x})\cos\left[2\left(\psi_0+0.81\,\lambda^2\int_z^L n_{\mathrm{e}}\,(B_{\|}+b_{\|})(\boldsymbol{x})\,dz'\right)\right]dz,\\
U(x_\perp) &= \int_0^L \varepsilon(\boldsymbol{x})\sin\left[2\left(\psi_0+0.81\,\lambda^2\int_z^L n_{\mathrm{e}}\,(B_{\|}+b_{\|})(\boldsymbol{x})\,dz'\right)\right]dz,\\
P(x_\perp) &= \sqrt{Q^2(x_\perp)+U^2(x_\perp)},
\end{aligned}$$

where the synchrotron emissivity ε from each cell is given by

$$\varepsilon(\boldsymbol{x}) = \begin{cases} c\left(B_\perp+b_\perp\right)^2(\boldsymbol{x}) & \text{if } C=0 \text{ with } \delta_{n_{\mathrm{cr}}}=0,\\ c(\boldsymbol{x})\left(B_\perp+b_\perp\right)^2(\boldsymbol{x}) & \text{if } C\neq 0 \text{ with } \delta_{n_{\mathrm{cr}}}=0.2,\end{cases}$$

with c a constant proportional to the cosmic ray electron density n_{cr} defined in Eq. (2.2) and $B_\perp$ and $b_\perp$ ($\perp = \{x, y\}$) the regular and turbulent transverse magnetic field components in μG. Moreover, λ is the 'observing' wavelength (m), ψ_0 is the intrinsic polarization angle, dz' and dz are increments along the line of sight with positive direction pointing toward the observer, n_{e} is the thermal electron density taken to be a constant, L is the total path length (pc), and z denotes the location of each emitting source along the line of sight with $z = 0$ marking the location of the farthest source from the observer. The maximum turbulent cell size d affects Q, U, and P through the dispersion of RM within the simulated volume given by $\sigma_{RM} = 0.81\, n_{\mathrm{e}}\, b_{||}\, (L\, d)^{1/2}$. As a check, histograms of the maps reveal Gaussian distributions for I, Q, and U while the map of P has a Rician distribution, since it is the sum of two Gaussian distributions, as expected. Figure 2.1 shows example maps of the Stokes parameters. Stokes I appears 'patchy' while P evolves from 'patchy' to having one pixel wide 'canals' of low intensity values arising from abrupt changes in the polarization angle to 'grainy' (more power on small scales) with increasing wavelength. The structure of both Stokes Q and U are essentially the same.

2.2.4 Angular power spectrum

In order to quantify the structure in the total intensity and polarization maps and compare with observations, we calculate angular power spectra following Haverkorn et al. (2003) but do not use the APS approach since our models maximally cover 0.3% of the $\sim 41,000$ square degrees on the sky. Instead, we use the PS approach with PS(ℓ) a function of multipole ℓ where $\mathrm{PS}_X(\ell)$ is given by the square of the discrete Fourier transform (DFT) $\mathcal{F}$ of a variable X as $\mathrm{PS}_X(\ell) = |\mathcal{F}(X)|^2$ with the DFT computed via the FFT algorithm. The power spectrum of b is calculated in three dimensions while the power spectra of I, Q, U, and P are computed in two dimensions and averaged over azimuth in radial bins. The multipole spectral index α, defined as $\mathrm{PS}_X(\ell) \propto \ell^{-\alpha_X}$, is calculated from a log-log fit to the power spectrum as in Fig. 2.2.

2.3 Results

We first consider the model with standard parameters as defined in Section 2.2. PS of polarized intensity and Stokes Q at a range of observing frequencies, viz. 1 GHz, 700 MHz, 500 MHz, 350 MHz, 200 MHz and 50 MHz are shown in Fig 2.2. Since the PS become very noisy at large angular scales (small multipoles), due to our limited simulation box size, we only consider multipoles $\ell \gtrsim 150$. At high frequencies (1 GHz and 700 MHz), the PS show an unbroken power law with a spectral index $\alpha_Q, \alpha_P \sim 2.8$ ($\alpha_b = 5/3$). However, at lower frequencies (500 MHz and 350 MHz), the PS show a break, where the spectral index is consistent with the high-frequency PS at small angular scales, but flattens out at larger scales. At small angular scales, the PS amplitude increases while it decreases at large scales due to the flattening of the PS. The location of the break is also frequency dependent; the break occurs at smaller angular scales for lower frequencies. The flattening of the large-scale spectrum increases towards lower frequencies. At the

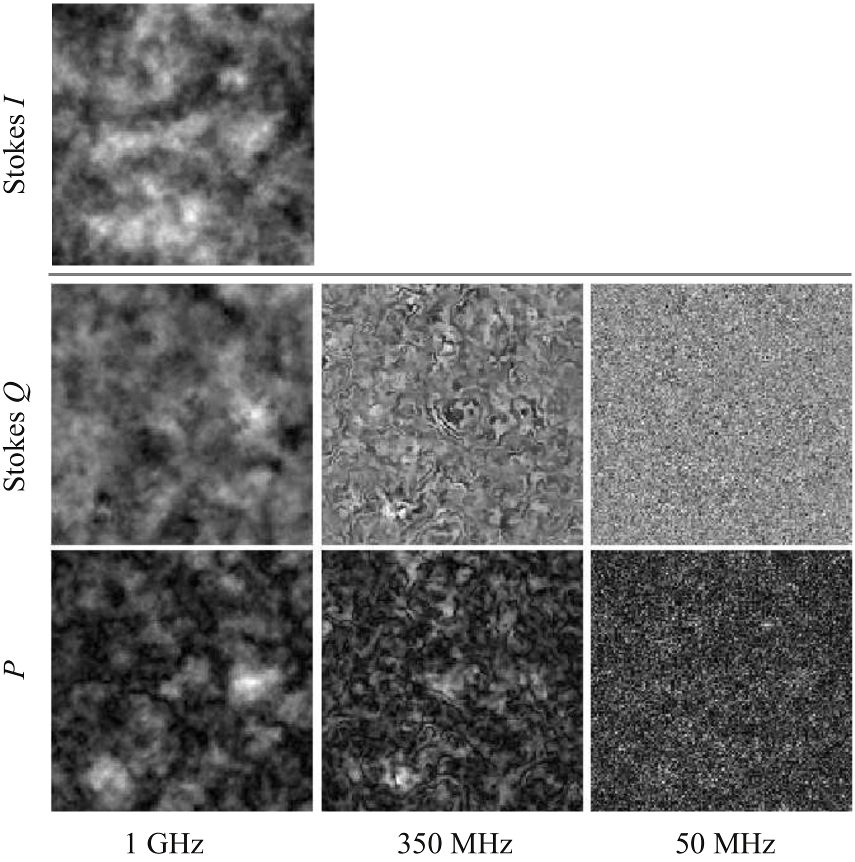

Figure 2.1: Sample simulated output map of Stokes I (top) and sample output maps of Stokes Q (middle) and P (bottom) observed at frequencies of 1 GHz, 350 MHz, and 50 MHz, respectively. All maps featured are for an input turbulent magnetic field power spectrum of $5/3$ for the choice of $B = 3\,\mu$G and $\sigma_b = 6\,\mu$G and $C = 0$, $\delta_{n_{\rm cr}} = 0$. A cone line of sight with 1 kpc distance has been used. Outer scale of turbulence is 100 pc. The gray scale range is independent for each parameter since this is more revealing of its structure with lighter shades corresponding to high values and darker shades to low values.

lowest frequencies (200 MHz and 50 MHz), the PS no longer show a break, but rather a flat to inverted PS. The flattening of the PS is more pronounced in the PS of Stokes Q than in P. Flattening of PS of polarized radio emission has been observed frequently (see Section 3.7) and has been explained by increased Faraday rotation and depolarization at low frequencies (Haverkorn et al. 2003). These simulation results show that there is a typical angular scale associated with a break in the PS, which is frequency dependent. In the following, we choose to work with the high spectral index, assuming that the steep part of the spectrum is representative.

Table 2.1: Output power spectral index of total intensity I, Stokes Q and polarized intensity P as a function of input power spectral index of turbulent magnetic field, α_b. The path length is 1 kpc and the outer scale of turbulence is 100 pc. The error in the spectral indices is the standard deviation of 10 independent realizations. The subscripts ‘st’ and ‘sh’ denote steep and shallow parts of the broken power spectrum observed at 350 MHz. The error is the standard deviation of 10 independent realizations. These values are given for positive and negative correlation between magnetic fields and cosmic rays represented by parameter C (see text) for $\boldsymbol{B} = 0$.

α_b	α_I	α_Q	α_P
$C = 0$			
$3/2_{\rm st}$	2.4 ± .1	1.2 ± .2	2.2 ± .2
$3/2_{\rm sh}$		.3 ± .2	1.2 ± .2
$5/3_{\rm st}$	2.5 ± .1	1.6 ± .2	2.5 ± .1
$5/3_{\rm sh}$		.4 ± .2	1.4 ± .3
$2_{\rm st}$	2.6 ± .2	2.3 ± .2	3.2 ± .2
$2_{\rm sh}$		.5 ± .2	1.8 ± .3
$C = -0.5$			
$3/2_{\rm st}$	2.2 ± .1	1.2 ± .2	2.0 ± .2
$3/2_{\rm sh}$		.3 ± .2	1.2 ± .2
$5/3_{\rm st}$	2.3 ± .1	1.6 ± .2	2.3 ± .1
$5/3_{\rm sh}$		.4 ± .2	1.3 ± .2
$2_{\rm st}$	2.3 ± .1	2.3 ± .2	2.9 ± .2
$2_{\rm sh}$		.5 ± .2	1.8 ± .3
$C = +0.5$			
$3/2_{\rm st}$	2.3 ± .1	1.2 ± .2	2.1 ± .2
$3/2_{\rm sh}$		.2 ± .2	1.2 ± .2
$5/3_{\rm st}$	2.4 ± .1	1.6 ± .2	2.5 ± .1
$5/3_{\rm sh}$		.4 ± .2	1.4 ± .3
$2_{\rm st}$	2.5 ± .2	2.3 ± .2	3.1 ± .2
$2_{\rm sh}$		.5 ± .2	1.9 ± .3
$C = -1$			
$3/2_{\rm st}$	2.4 ± .1	1.2 ± .1	2.1 ± .2
$3/2_{\rm sh}$		.3 ± .2	1.2 ± .2
$5/3_{\rm st}$	2.5 ± .1	1.6 ± .2	2.4 ± .1
$5/3_{\rm sh}$		.4 ± .2	1.3 ± .2
$2_{\rm st}$	2.7 ± .1	2.3 ± .2	3.1 ± .2
$2_{\rm sh}$		.5 ± .2	1.7 ± .2
$C = +1$			
$3/2_{\rm st}$	2.4 ± .1	1.2 ± .2	2.2 ± .3
$3/2_{\rm sh}$		.2 ± .2	1.2 ± .2
$5/3_{\rm st}$	2.5 ± .1	1.6 ± .2	2.5 ± .1
$5/3_{\rm sh}$		.4 ± .2	1.5 ± .3
$2_{\rm st}$	2.6 ± .2	2.3 ± .2	3.2 ± .2
$2_{\rm sh}$		.5 ± .2	1.9 ± .3

Table 2.2: As in Table 2.1 but for an outer scale of 50 pc.

α_b	α_I	α_Q	α_P
$C = 0$			
$3/2_{\mathrm{st}}$	2.4 ± .1	.6 ± .1	1.6 ± .2
$3/2_{\mathrm{sh}}$		−.3 ± .1	.3 ± .1
$5/3_{\mathrm{st}}$	2.6 ± .1	.7 ± .2	1.8 ± .1
$5/3_{\mathrm{sh}}$		−.2 ± .2	.3 ± .1
2_{st}	2.8 ± .1	1.1 ± .1	2.2 ± .2
2_{sh}		−.2 ± .2	.5 ± .1

Table 2.3: As in Table 2.1 but for an outer scale of 100 pc and path length of 2 kpc. The error is the standard deviation of 5 independent realizations.

α_b	α_I	α_Q	α_P
$C = 0$			
$3/2_{\mathrm{st}}$	2.3 ± .2	.1 ± .1	1.2 ± .2
$3/2_{\mathrm{sh}}$		−.6 ± .2	0. ± .2
$5/3_{\mathrm{st}}$	2.6 ± .1	.3 ± .1	1.4 ± .1
$5/3_{\mathrm{sh}}$		−.6 ± .2	.3 ± .1
2_{st}	2.6 ± .1	.6 ± .1	1.9 ± .1
2_{sh}		−.6 ± .2	.5 ± .1

Table 2.4: As in Table 2.3 but for an outer scale of 50 pc and path length of 2 kpc.

α_b	α_I	α_Q	α_P
$C = 0$			
$3/2_{\mathrm{st}}$	2.4 ± .1	−.4 ± .1	.6 ± .1
$3/2_{\mathrm{sh}}$		−.5 ± .2	−.3 ± .2
$5/3_{\mathrm{st}}$	2.5 ± .1	−.1 ± .1	.9 ± .1
$5/3_{\mathrm{sh}}$		−.5 ± .1	−.2 ± .2
2_{st}	2.8 ± .1	−.1 ± .1	1.2 ± .1
2_{sh}		−.6 ± .2	0. ± .2

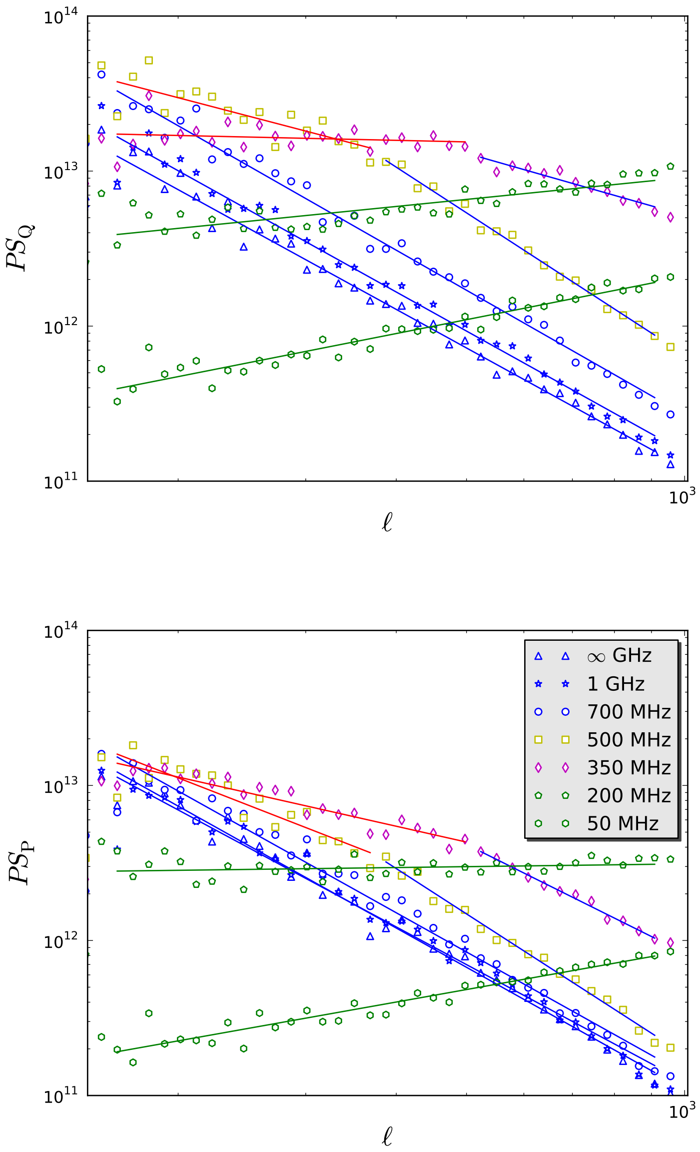

Figure 2.2: Angular power spectra of Stokes Q (right) and polarized intensity P (left) in simulations with $\alpha_b = 5/3$ and standard parameters (see text), for a range of observing frequencies for $\boldsymbol{B} = 0$ and $C = 0$. In the presence of a break, the red and blue solid lines give the best-fit slope for the shallow and steep parts, respectively.

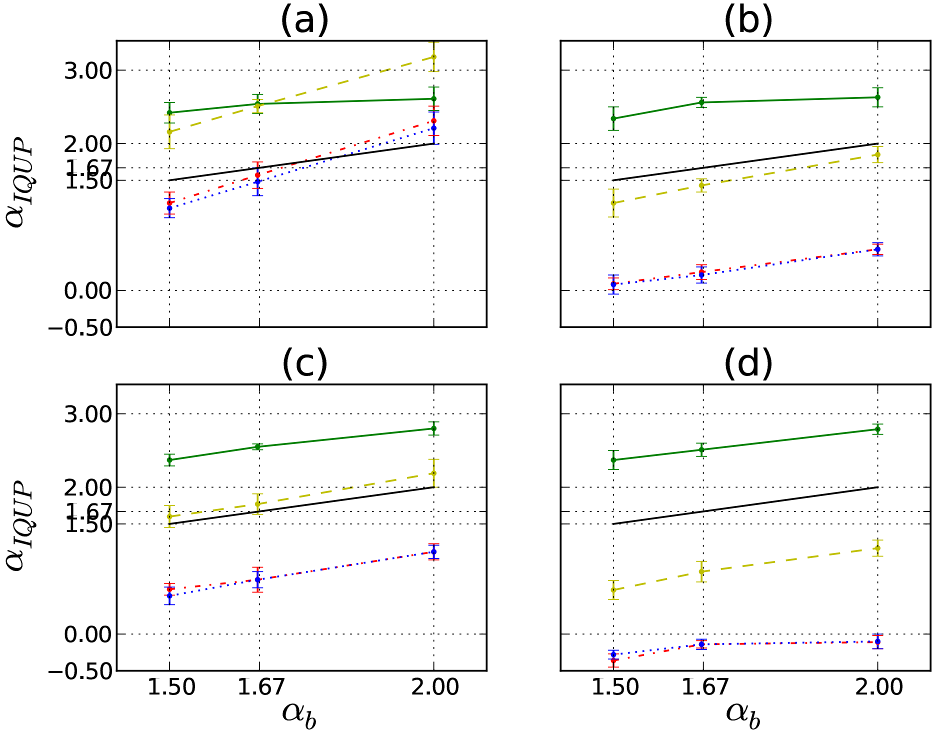

Figure 2.3: Trends of angular power spectra of I, Q, U, and P for input turbulent magnetic field power spectra $\boldsymbol{b}$ at 350 MHz for $\boldsymbol{B} = 0$ and $C = 0$. The solid green line corresponds to α_I, the dashed yellow line to α_P, the red dash dotted line to α_Q, and the blue dotted line to α_U. The solid black line indicates the locus of equality. The following trends are shown: (a) path length of 1 kpc and an outer scale of turbulence of 100 pc, (b) path length of 1 kpc and an outer scale of turbulence of 50 pc, (c) path length of 2 kpc and an outer scale of turbulence of 100 pc, (d) path length of 2 kpc and an outer scale of turbulence of 50 pc. In all these plots, only the steep part of the spectrum has been plotted.

2.3.1 Dependence on magnetic field spectral index

The spectral index of PS of polarized emission should depend on the spectral index of the input turbulent magnetic field. Whether this dependence is unique and whether it can be observed is a crucial question. If this is possible, then we can directly determine magnetic field spectral indices from radiopolarimetric observations. The dependence of spectral indices of I, Q, U and P on the spectral index of the input random, isotropic Gaussian magnetic fields are shown in Fig. 2.3 for our standard frequency of 350 MHz. The four plots show the variation with path length through the medium (1 kpc and 2 kpc) and with outer scale of turbulence (50 pc and 100 pc). All respective spectral index values for these plots are provided in Tables 2.1 - 2.4.

Table 2.5: As in Table 2.1 for $\boldsymbol{B} = 0$ and $C = 0$ but for observing frequencies of 1 GHz and 50 MHz.

α_b	α_I	α_Q	α_P
1 GHz			
3/2	$2.4 \pm .1$	$2.6 \pm .1$	$2.6 \pm .1$
5/3	$2.5 \pm .1$	$2.7 \pm .1$	$2.7 \pm .1$
2	$2.6 \pm .2$	$2.8 \pm .1$	$3. \pm .1$
			$^{*}\,2.4 \pm .2$
50 MHz			
3/2	$2.4 \pm .1$	$-1. \pm .1$	$-.9 \pm .1$
5/3	$2.5 \pm .1$	$-1. \pm .1$	$-.9 \pm .1$
2	$2.6 \pm .2$	$-1. \pm .1$	$-.8 \pm .1$

Notes: $^{(*)}$ $B_\perp$

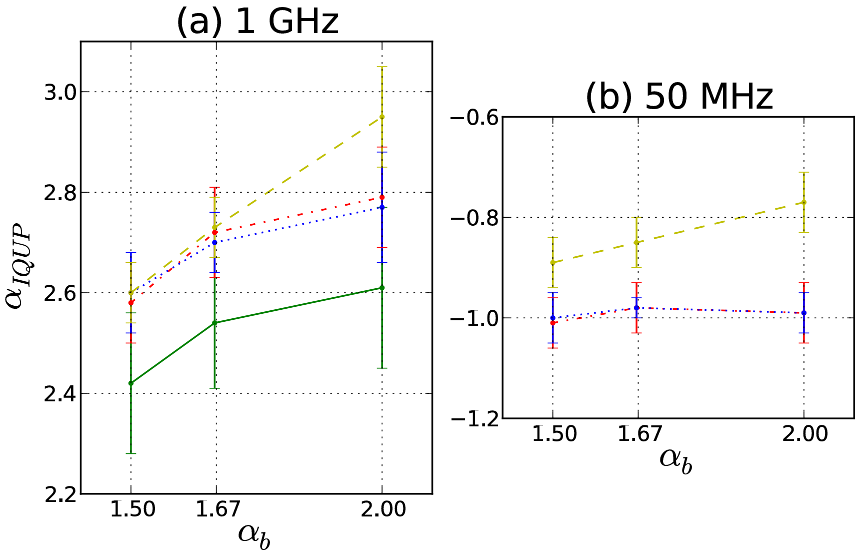

Figure 2.4: Trends of angular power spectra of I, Q, U, and P for $\boldsymbol{B} = 0$ and $C = 0$ at a frequency of 1 GHz (a) and 50 MHz (b). The path length is 1 kpc and the outer scale of turbulence is 100 pc. The legend is the same as in Fig. 2.3. Since α_I is not frequency dependent it is not reproduced in (b).

The spectral indices of I, Q, U, and P increase with increasing α_b as expected. In order to explain our results for the spectral index of I we argue along the following lines. For $\alpha_b = 5/3$ in 1D, one would expect a 3D magnetic field PS of $\alpha_b = 11/3$. Since synchrotron intensity (Stokes I) is the *addition* of emissivity due to these fields along a line of sight, and not an integration over scale k, the spectral index of the 2D Stokes I map should also be $\alpha_I^{2D} = 11/3$. Integrating the Stokes I map to a one-dimensional PS will thus result in $\alpha_I = 8/3$. By analogy, we might expect that $\alpha_I = \alpha_b + 1$ which is supported by our simulations. The spectral index of Stokes I does not depend on outer scale of turbulence or path length, as expected.

Spectral indices of polarized radiation depend on path length and turbulent outer scale, because these change the depolarization characteristics. As expected, $\alpha_Q = \alpha_U$. The spectral indices of Q, U and P increase with increasing α_b, but there is no fixed relation as for α_I. In all situations presented in Fig. 2.3, $\alpha_P > \alpha_Q, \alpha_U$, which means that in Q and U, turbulence creates more small-scale structure than in P.

Polarization spectral indices at 1 GHz and 50 MHz are given in Table 2.5 and Fig. 2.4. At 1 GHz, $\alpha_I \approx \alpha_P \approx \alpha_Q \approx \alpha_U$, indicating that Faraday rotation and depolarization only play a minor role at this frequency. This was also noted observationally at 1.4 GHz (Stutz et al. 2014). In fact, Fig. 2.2 indicates that complete depolarization already occurs at 1 GHz since α_I has the same spectral index as at $\lambda = 0$ (∞ frequency).

2.3.2 Dependence on other input parameters

Figure 2.3 shows the dependence of output spectral indices on path length. Doubling the path length from 1 kpc to 2 kpc does not change the spectrum of Stokes I. However, the spectra of polarized emission (Q, U, and P) become considerably shallower. This result is consistent with the additional depolarization resulting from a longer path length, which converts large scale structure into small scales. Similarly, decreasing the maximum scale of magnetic field fluctuations from 100 pc to 50 pc leads to a shallowing of the polariztion spectra.

Introducing a correlation or anti-correlation between the magnetic field energy density and cosmic ray density by the factor C (see Section 2.2.2) does not alter polarization spectral indices as seen from Table 2.1, but has an effect on the amplitude of the PS, as shown in Fig. 2.5. However, the PS of I for $C = -0.5$ is flatter than for other values of C which is due to an upturn at the smallest scales as seen in panel (a) of the same figure. The largest amplitude in I and P (and similarly for Q and U) arises from equipartition ($C = 1$) whereas the lowest comes from pressure equilibrium ($C = -1$). Since the (anti-)correlation indicates a dependence of $n_{\rm cr}$ on $\boldsymbol{B}_{\rm tot}$ as in Eq. 2.2, this is indeed as expected. Therefore, spectral index studies cannot be used to determine the rate of correlation between magnetic field and cosmic rays in the interstellar medium. Additionally, spectral indices are found to be insensitive to either the presence or the orientation of the regular field $\boldsymbol{B}$ for the regular and turbulent magnetic field strengths considered here.

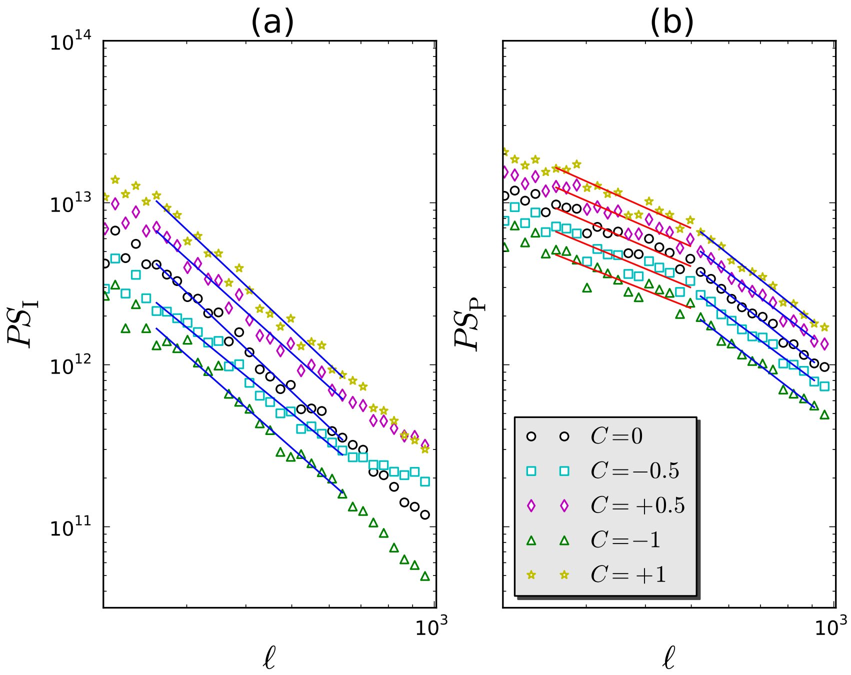

Figure 2.5: Amplitudes of the power spectra of I (a) and P (b) at 350 MHz for $C = 0, \pm0.5, \pm1$ (see text), $\alpha_b = 5/3$, and standard parameters.

2.4 Discussion

The aim of this chapter is to establish the dependence of spectral indices of total and polarized intensity and Stokes parameters Q and U on physical parameters in the ISM. Our simulations suggest that total intensity Stokes I is a good tracer of the underlying magnetic field power spectrum as long as magnetic field fluctuations dominate over thermal density fluctuations in the real ISM. However, it may not be possible to distinguish between different α_b using α_I.

Regis (2011) computes Stokes I power spectra for five radio surveys from the literature and finds $\alpha_I = 2.9^{+0.3}_{-0.1}$ for high latitudes, in agreement with our findings of α_I for a spectrum with $\alpha_b = 2$. However, as Regis expects α_I to reproduce the 3D Kolmogorov spectrum of thermal density fluctuations (i.e. $\alpha_I = 11/3$), he concludes that his value of α_I is shallower.

Depolarization has been named as a cause of flattening of power spectra of polarized emission in a number of observational papers (e.g. Baccigalupi et al. (2001); Haverkorn et al. (2003)). We confirm numerically that depolarization flattens the power spectra of the polarized emission. However, since depolarization depends degenerately on many factors such as path length, turbulent magnetic field, or outer scale of fluctuations, spectral indices of Q, U or P cannot be used to determine the spectral index of turbulent magnetic field. In fact, a large variety of spectral indices of polarized emission is expected to occur even for a single turbulent magnetic field spectrum. A wide range of α_P is indeed observed in the Canadian Galactic Plane Survey and its vertical extensions by Stutz et al. (2014). These authors find an average $\langle\alpha_P\rangle = 2.3$ with significant spatial variation. Their conclusion that α_P increases with Galactic latitude may be a path length effect as shown in our simulations.

Their study also finds that $\alpha_P = \alpha_Q = \alpha_U$ at 1.4 GHz, in agreement with our results. Our simulations also confirm the observed flattening of α_P as a function of observing wavelength (Haverkorn et al. 2003). The simulation result that $\alpha_P > \alpha_Q, \alpha_U$ is generally not confirmed by observations. At low frequencies, $\alpha_P < \alpha_Q, \alpha_U$ is observed (Haverkorn et al. 2003). However, the steepening of α_Q, α_U is attributed to the presence of nearby Faraday screens: these screens will add large-scale structure to Q and U, but not to P. Since our simulation does not contain Faraday screens, we cannot hope to reproduce these observational results.

We show, to our knowledge for the first time, that the PS of Q, U, and P may have a frequency dependent break. The frequency dependence of the angular scale of the break depends on parameters of the turbulence such as magnetic field strength, path length, and thermal electron density. Therefore, measuring the angular scale of the break as a function of frequency may help determine the turbulence parameters. This should be accompanied by simulations testing the dependence of the angular scale of the break on turbulence parameters, which is beyond the scope of this chapter.

An interesting prediction of our simulations is the flattening of the PS at very low frequencies. This means that low-frequency polarimetric observations from e.g. LOFAR or the MWA may seem pure noise, but may contain signal. Polarized intensity PS constructed at very low frequencies should in theory show an inverted power spectrum (to a positive slope). However, in practice this may be difficult to observe due to the low PS amplitude and finite observing beams.

2.5 Summary and conclusions

We constructed static simulations of the magneto-ionized ISM using a power spectrum of random magnetic field with random phases and a predetermined spectral index, constant thermal electron density, and cosmic ray density that can be either constant or (anti-) correlated with magnetic energy density. We simulate radiopolarimetric observations by calculating the propagation of polarized synchrotron radiation through the medium and study the resulting spectral indices α of Stokes I, Q, U and polarized intensity P as a function of magnetic field power spectrum, path length, outer scale of turbulence, correlation of cosmic rays and magnetic field, and frequency.

Our models confirm that more depolarization leads to shallower spectra, where depolarization can be increased by increasing path length or decreasing frequency. We show that smaller outer scales of turbulence lead to smaller α_P, but that (anti-) correlation of magnetic field and cosmic rays does not have a discernible influence on α_P. The dependence of polarization spectral index on ISM parameters indicates that the variety in α_P in observations, even within the same survey, can originate in a single spectrum of magnetic field. Polarization power spectra not only flatten with decreasing frequency, but show a break at mutipoles that increase with decreasing frequency. At very low frequencies ($\lesssim$ 200 MHz), this can lead to flat or even inverted power spectra. This behavior may become visible with the current low-frequency instruments such as LOFAR or MWA.

Acknowledgements

CS and MH acknowledge the support of research program 639.042.915, which is partly financed by the Netherlands Organization for Scientific Research (NWO). CS is grateful for the additional financial support by the *Leids Kerkhoven-Bosscha Fonds, LKBF* work visit subsidies. AF and AS thank the Leverhulme trust for financial support under grant RPG-097. The simulations were performed on the Coma Cluster at Radboud University, Nijmegen, The Netherlands.

Bibliography

Armstrong, J. W., Rickett, B. J., & Spangler, S. R. 1995, ApJ, 443, 209

Baccigalupi, C., Burigana, C., Perrotta, F., et al. 2001, A&A, 372, 8

Beresnyak, A. 2014, ApJ, 784, L20

Beresnyak, A. & Lazarian, A. 2006, ApJ, 640, L175

Bowman, J. D., Cairns, I., Kaplan, D. L., et al. 2013, PASA, 30, 31

Bruscoli, M., Tucci, M., Natale, V., et al. 2002, New A, 7, 171

Burn, B. J. 1966, MNRAS, 133, 67

Carretti, E., Haverkorn, M., McConnell, D., et al. 2010, MNRAS, 405, 1670

Chepurnov, A. & Lazarian, A. 2010, ApJ, 710, 853

Cho, J. & Lazarian, A. 2003, MNRAS, 345, 325

de Bruyn, A. G., Katgert, P., Haverkorn, M., & Schnitzeler, D. H. F. M. 2006, Astronomische Nachrichten, 327, 487

Gaensler, B. M., Madsen, G. J., Chatterjee, S., & Mao, S. A. 2008, PASA, 25, 184

Galtier, S., Pouquet, A., & Mangeney, A. 2005, Physics of Plasmas, 12, 092310

Han, J. 2009, in IAU Symposium, Vol. 259, IAU Symposium, ed. K. G. Strassmeier, A. G. Kosovichev, & J. E. Beckman, 455–466

Haverkorn, M. & Heesen, V. 2012, Space Sci. Rev., 166, 133

Haverkorn, M., Katgert, P., & de Bruyn, A. G. 2003, A&A, 403, 1045

Haverkorn, M., Katgert, P., & de Bruyn, A. G. 2004, A&A, 427, 169

Heald, G. & LOFAR Collaboration. 2014, in American Astronomical Society Meeting Abstracts, Vol. 223, American Astronomical Society Meeting Abstracts, 236.07

Jansson, R. & Farrar, G. R. 2012, ApJ, 761, L11

Jelić, V., Zaroubi, S., Labropoulos, P., et al. 2008, MNRAS, 389, 1319

La Porta, L. & Burigana, C. 2006, A&A, 457, 1

La Porta, L., Burigana, C., Reich, W., & Reich, P. 2008, A&A, 479, 641

Malik, N. A. & Vassilicos, J. C. 1999, Physics of Fluids, 11, 1572

Regis, M. 2011, Astroparticle Physics, 35, 170

Schnitzeler. 2008, PhD thesis, Leiden University, The Netherlands

Shneider, C., Haverkorn, M., Fletcher, A., & Shukurov, A. 2014, A&A, 567, A82

Simonetti, J. H., Cordes, J. M., & Spangler, S. R. 1984, ApJ, 284, 126

Sokoloff, D. D., Bykov, A. A., Shukurov, A., et al. 1998, MNRAS, 299, 189

Sokoloff, D. D., Bykov, A. A., Shukurov, A., et al. 1999, MNRAS, 303, 207
Stepanov, R., Shukurov, A., Fletcher, A., et al. 2014, MNRAS, 437, 2201
Stutz, R. A., Rosolowsky, E. W., Kothes, R., & Landecker, T. L. 2014, ApJ, 787, 34
Sun, X. H. & Reich, W. 2009, A&A, 507, 1087
Tucci, M., Carretti, E., Cecchini, S., et al. 2002, ApJ, 579, 607
Weisstein, E. W. 2002, Sphere Point Picking, http://mathworld.wolfram.com
Wieringa, M. H., de Bruyn, A. G., Jansen, D., Brouw, W. N., & Katgert, P. 1993, A&A, 268, 215
Wilkin, S. L., Barenghi, C. F., & Shukurov, A. 2007, Physical Review Letters, 99, 134501
Wilkin, S. L. 2006, PhD thesis, Newcastle University, U.K.
Zweibel, E. G. & Heiles, C. 1997, Nature, 385, 131